

Journal of Materials Chemistry A

Materials for energy and sustainability

Accepted Manuscript

This article can be cited before page numbers have been issued, to do this please use: G. I. Almerindo, S. Buratto, E. H. Wanderlind, L. M. Nicolazi, P. Sangaletti, M. Medeiros, F. S. S. Schneider, G. F. Caramori, R. L. T. Parreira, G. A. Micke and H. D. Fiedler, *J. Mater. Chem. A*, 2020, DOI: 10.1039/C9TA14028J.



This is an Accepted Manuscript, which has been through the Royal Society of Chemistry peer review process and has been accepted for publication.

Accepted Manuscripts are published online shortly after acceptance, before technical editing, formatting and proof reading. Using this free service, authors can make their results available to the community, in citable form, before we publish the edited article. We will replace this Accepted Manuscript with the edited and formatted Advance Article as soon as it is available.

You can find more information about Accepted Manuscripts in the [Information for Authors](#).

Please note that technical editing may introduce minor changes to the text and/or graphics, which may alter content. The journal's standard [Terms & Conditions](#) and the [Ethical guidelines](#) still apply. In no event shall the Royal Society of Chemistry be held responsible for any errors or omissions in this Accepted Manuscript or any consequences arising from the use of any information it contains.

ARTICLE

Kinetics and Adsorption Calculations: Insights into the MgO-Catalyzed Detoxification of Simulants of Organophosphorus Biocides

Received 00th January 20xx,
Accepted 00th January 20xx

DOI: 10.1039/x0xx00000x

Gizelle I. Almerindo,^{a,b,*} Suelen C. Buratto,^c Eduardo H. Wanderlind,^{c,d,*} Lucas M. Nicolazi,^c Patrícia Sangaletti,^c Michelle Medeiros,^c Felipe S. S. Schneider,^c Giovanni F. Caramori,^c Renato L. T. Parreira,^e Gustavo A. Micke,^c Haidi D. Fiedler^{c,*} and Faruk Nome^{c,†}

We report the targeted decomposition of the organophosphate methyl paraoxon by means of its transesterification with 1-propanol catalyzed by magnesium oxide. Catalyst characterization by energy dispersive X-ray fluorescence (EDXRF), nitrogen adsorption/desorption measurements (BET and BJH methods), and temperature programmed desorption of CO₂ (CO₂-TPD) showed that the employed MgO presents properties favorable for the methyl paraoxon adsorption and for the transesterification to occur. A thorough kinetic investigation showed that rate enhancements up to 3 × 10⁶-fold can be achieved in comparison with the spontaneous propanolysis of the substrate, and that the material can be used in additional cycles without loss of catalytic activity, being the catalyst recovery attained through a simple washing procedure. Adsorption energies for 1-propanol and methyl paraoxon onto a MgO model surface were obtained by density functional theory calculations, which showed that the latter displays a stronger affinity with the catalyst surface, and that the reaction should proceed with methyl paraoxon and 1-propanol molecules juxtapositioned at adjacent Mg²⁺ sites, with nucleophilic and electrophilic centers c.a. 2.4 Å distant from each other. Additionally, MgO also promoted rate enhancements up to 5 × 10⁴-fold in the propanolysis of a further range of representative phosphate triesters, and in most of the cases the final transesterified products are trialkyl phosphates structurally related to a family of flame-retardants. The results thus provide insights into the development of novel systems for the targeted conversion of organophosphorus compounds into value-added products by employing simple, highly efficient, and low cost metal oxide catalysts.

1. Introduction

Organophosphorus compounds are amongst the most toxic classes of compounds to the human being, primarily because of the inhibition of acetylcholinesterase activity in the nervous system.^{1–3} This mechanism of action has led to the development in the past of highly potent nerve agents for military applications, requiring the investigation of methodologies for the safe and effective decomposition of stockpiles of such compounds.^{1,4–6} This is because most of the preferred methodologies currently employed for the destruction of these

nerve agents, which include incineration and alkaline hydrolysis, are not convenient to effectively detoxify a large body of substrates, presenting in many instances disadvantages such as the formation of toxic by-products.^{1,4,6} In the continuous effort for the development of methodologies for the detoxification of organophosphorus compounds, researches have focused on the development of catalytic systems as effective means to accelerate a given targeted reaction.^{1,4}

Indeed, there is a number of recent examples in the literature highlighting a variety of catalytic systems designed for the cleavage of organophosphorus compounds as well as their simulants, frequently used in worldwide laboratories as a precautionary measure due to the high toxicity of the substrates. These include homogeneous^{7–12} and microheterogeneous^{13–18} systems, displaying different modes of catalysis in a diverse range of systems including, for example, metal complexes, polymers, metallic nanoparticles, ionic liquids, etc. Significantly, developing mechanistic understanding of enzymes that exhibit phosphotriesterase activity promises improved medical treatments for cases of intoxication by organophosphorus compounds.^{19–21}

Additionally, a great number of heterogeneous systems is also reported.^{22–29} Heterogeneous catalysis has proved to be of great value in the detoxification of organophosphorus compounds, since it provides decisive practical features

^a Faculdade de Engenharia Química, Escola do Mar, Ciência e Tecnologia, Universidade do Vale do Itajaí (UNIVALI), 88302-901, Itajaí, Santa Catarina (SC), Brazil. E-mail: gizelle.almerindo@univali.br (G.I.A)

^b Programa de Pós-Graduação em Ciências Farmacêuticas, Universidade do Vale do Itajaí (UNIVALI), 88302-901, Itajaí, Santa Catarina (SC), Brazil.

^c Departamento de Química, Universidade Federal de Santa Catarina (UFSC), 88040-900, Florianópolis, Santa Catarina (SC), Brazil. E-mail: haidi.fiedler@ufsc.br (H.D.F)

^d Institute of Chemistry, University of Campinas (UNICAMP), 13083-970, Campinas, São Paulo, Brazil. Emails: ewanderlind@gmail.com or ehw@unicamp.br (E.H.W)

^e Núcleo de Pesquisas em Ciências Exatas e Tecnológicas, Universidade de Franca, Franca, SP, 14404-600, Brazil.

† F.N. is deceased since Sept. 24, 2018.

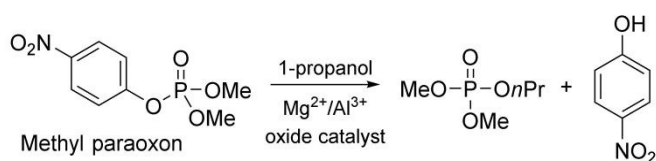
Electronic Supplementary Information (ESI) available: Data of characterization of solids, kinetic measurements, identification of products, and Cartesian coordinates, as well as energies, of structures studied by DFT. See DOI: 10.1039/x0xx00000x

compared with homogeneous media, such as convenient separation of the catalyst and its recycling.^{30–32} More specifically, metal oxides attract particular attention because they are simple, robust catalysts known to be highly active while being stable in a wide range of temperatures.^{1,33} Several reports highlight the catalytic activity of simple metal oxides toward the solvolysis of organophosphorus compounds, hydrolysis being the most studied reaction,^{34–38} with a lower number of examples of solvolysis by alcohols.^{39–41} Besides the acid-base properties of the metal oxides, their geometric and textural properties, as well as the nature of the metal, are intrinsically related to the catalytic effect. Thus, researchers have directed efforts into the use of solids that present proper geometric and textural arrangements for a targeted mechanism of catalysis.

In this sense, we investigated recently the propanolysis reaction of methyl paraoxon (dimethyl 4-nitrophenyl phosphate) catalyzed by a series of mixed Mg^{2+}/Al^{3+} oxides (Scheme 1).⁴² The solid featuring an incipient spinel phase showed to be the most active one, leading to rate enhancements of ca. 2.5×10^5 -fold in comparison to the spontaneous propanolysis of the substrate.⁴² Significantly, the transesterification of methyl paraoxon leads to a product structurally related to a family of flame-retardants of particular interest, since the use of trialkyl organophosphate esters has increased considerably as substitutes for environmentally persistent flame-retardants currently employed by the industry.⁴³ Also, the incipient $MgAl_2O_4$ spinel showed to be highly efficient in the propanolysis of a wide range of phosphate triesters, including dialkyl aryl, alkyl diaryl and triaryl substrates, evidencing that the catalytic effect depends on the nature of the triester substituents.⁴⁴

Additionally, we also focused in the evaluation of the effect of lanthanide metal centers in solid catalysts: a novel aluminum-titanate-supported erbium oxide promoted catalytic effects of at least 7×10^5 -fold in the propanolysis of methyl paraoxon.⁴⁵ And more recently, we described the greatest catalytic effect reported so far for this target reaction: a 10^7 -fold effect, achieved with a catalyst of strontium alkaline compounds featuring strontium oxide as main component, being the superior catalytic effect well correlated to the strong base site density of the material surface.⁴⁶

Envisioning the application of metal oxides in the decomposition of organophosphorus compounds, we report herein an investigation of the model magnesium oxide (MgO) as catalyst in the propanolysis of methyl paraoxon and a further range of phosphate triesters. Additionally, the experimental results are complemented with density functional theory calculations employed to obtain adsorption energies and gain insights into the reaction mechanism.



Scheme 1 Propanolysis of methyl paraoxon catalyzed by mixed $MgAl_2O_4$ oxides.

2. Experimental

Materials

Magnesium oxide (Vetec; lot 021953) and γ -alumina (Merck; lot TA1328576-542) were purchased and used as received. The phosphate triesters used in this study, methyl paraoxon (dimethyl 4-nitrophenyl phosphate), dimethyl 2,4-dinitrophenyl phosphate (DMDNPP), diethyl 2,4-dinitrophenyl phosphate (DEDNPP), *tris*-2-pyridyl phosphate (T2PyP), and *tris*-4-nitrophenyl phosphate (T4NPP), were all synthesized as described previously (experimental procedures and characterization data are presented in the ESI), except for chlorpyrifos methyl *O*-analog (CPO), which was purchased (Sigma Aldrich) and used as received. Doubly deionized water with conductance $< 5.6 \times 10^{-8} \Omega^{-1} \text{ cm}^{-1}$ and pH 6.0–7.0 used to prepare reagent solutions was from a NANOpure analytical deionization system (type D-4744).

Catalyst Characterization

Thermogravimetric analysis (TGA). The thermogravimetric analyses were carried out using a Shimadzu TGA-50 analyzer, under an airflow of 20 mL min^{-1} , with heating from 25 to $800 \text{ }^\circ\text{C}$ under oxidizing atmosphere and heating rate of $10 \text{ }^\circ\text{C min}^{-1}$.

Energy Dispersive X-Ray Fluorescence (EDXRF). Analyses of EDXRF were performed in a Bruker S2 Ranger instrument and the software EQUA-OXIDES was used for instrument control, and data collection and analysis. Samples were analyzed as pressed pellets following the procedures of ASTM D2216.^{47,48}

Nitrogen Adsorption/Desorption Isotherms. Measurements of nitrogen adsorption and desorption were performed at $-196 \text{ }^\circ\text{C}$ using a Quantachrome Nova 2200e instrument. The samples were degassed at $300 \text{ }^\circ\text{C}$ under vacuum for 1 h. Specific surface areas were calculated according to the Brunauer–Emmett–Teller (BET) method, and the total pore volume and pore size distributions were obtained according to the Barret–Joyner–Halenda (BJH) method.⁴⁹

Temperature Programmed Desorption of CO_2 (CO_2 -TPD). The CO_2 -TPD analyses were performed using a Quantachrome ChemBET 3000 instrument. The samples were treated in situ under a helium atmosphere (100 mL min^{-1}) at $500 \text{ }^\circ\text{C}$ for 1 h before cooling to room temperature, and then the samples were saturated with $100 \text{ mL CO}_2 \text{ min}^{-1}$ for 40 min. After, physically adsorbed CO_2 was purged by a helium flow at room temperature for 30 min. CO_2 -TPD were carried out in a stream of helium (100 mL min^{-1}) with a heating rate of $10 \text{ }^\circ\text{C min}^{-1}$ reaching a final temperature of $800 \text{ }^\circ\text{C}$.

Catalyst Activity: Kinetic Measurements

Typically, the reactions were performed as follows: 20 mL of dried 1-propanol (stored with 3 \AA molecular sieves) were mixed with 300 mg of pre-dried catalyst ($450 \text{ }^\circ\text{C}/45 \text{ min}$), and the reaction was started by adding an aliquot of a stock solution of the substrate (in acetonitrile, stocked in freezer) under continuous magnetic stirring and argon atmosphere, the system being sealed with a rubber septum. All the reactions were performed employing previously optimized stirring velocity and reaction temperature of 640 rpm and $80 \text{ }^\circ\text{C}$, respectively (for

details, see the ESI). In order to monitor the kinetics of the reactions, appropriate aliquots of the reaction media were withdrawn periodically and added to a solvent mixture of 0.2 mL of ethanol and 0.2 mL of tris buffer at pH 9.0 containing NaCl 4.0 mol L⁻¹. The mixture was stirred in a vortex and sequentially centrifuged. Then, 0.7 mL of supernatant solution were transferred to a quartz cuvette and diluted with a mixture of 0.2 mL of ethanol and 1.5 mL of water, and absorbance changes were followed at the specific wavelength of the phenolic products by recording UV-Vis spectra with a Hewlett-Packard HP-8453 UV-Vis spectrophotometer. For methyl paraoxon specifically, a set of experiments was performed with different ratios of moles of substrate per mass unit of catalyst from 5 × 10⁻⁶ to 5 × 10⁻³ mol g⁻¹, by adjusting both the concentration of methyl paraoxon in the reaction media and the mass of the catalyst to achieve the desired final ratio. The propanolysis reactions of a series of representative phosphate triesters catalyzed by MgO were performed as described in the general procedure above employing 4.6 × 10⁻⁵ mol g⁻¹ (substrate/catalyst).

Characterization of products

The phenolic products were determined quantitatively by UV-Vis spectrophotometry using a Hewlett-Packard HP-8453 instrument. The transesterified products were characterized using high performance liquid chromatography coupled to mass spectrometry. An Allcrom Synergi™ 4 μm Polar RP column (150 mm length; 2.0 mm diameter) was employed with a flux of 200 μL/min at 25 °C using an Applied Biosystems/MDS SCIEX 3200 Q TRAP® LC/MS/MS System.

Catalyst recycling

At a ratio of 4.6 × 10⁻⁵ mol g⁻¹, propanolysis of methyl paraoxon was performed three times consecutively using the same starting MgO. The reactions and kinetic data treatment were performed as described above. Between reactions the catalyst was subjected to a reactivation procedure as follows. MgO was washed with deionized water five times being centrifuged after each wash, and this procedure was performed sequentially with a solution of NaCl 4 mol L⁻¹. Then, MgO was washed once with deionized water, vacuum filtrated and dried at 120 °C/5h. Post characterization of MgO was performed by TGA, EDXRF and nitrogen adsorption/desorption measurements.

Computational methods

In order to investigate the adsorption process of reactants, quantum chemical calculations were employed, which were done using slab calculations (revPBE-D3BJ/DZP⁵⁰) as implemented in ADF⁵¹ (version 2019.103). Bulk, single unit cell, periclase (MgO) calculations were carried out with an initial experimental⁵² cell constant of 4.210 Å, which was allowed to relax completely (final cell constant of 4.212 Å). A single surface unit cell, 6-atom thick periodic slab model of the (100) surface of the bulk structure, had half its outermost layers relaxed, the other atoms being held fixed. A 14.884 × 14.884 Å² (Mg₁₅₀O₁₅₀) clear cut was further optimized and employed as a supercell slab for representing the surface, always holding the innermost

3-atom layer fixed but relaxing the rest. The same box dimensions were employed in all calculations. 1-Propanol, 1-propoxide, and the phosphate educt were fully optimized on this surface. The semi-relaxed surface, as well as gas-phase optimizations of the adsorbents, were used in the calculation of adsorption energies. For 1-propoxide, a proton was added bound to the oxygen closest to the adsorbent in order to create the most stable ion pair possible.

3. Results and discussion

Catalyst Characterization

Since the catalytic activity of solid materials is intrinsically related to textural and acid-base properties, the commercial MgO was initially subjected to a series of characterization techniques. Firstly, TGA analysis shows a mass reduction of 15% with increasing temperature up to 400 °C, above which residual materials, probably water and CO₂, are fully eliminated (TGA profile is shown in Figure S1 in the ESI). Thus, standard thermic activation involved degassing the MgO at 450 °C before performing the reactions for catalytic activity evaluation. Additionally, the composition of MgO was verified by semi-quantitative EDXRF analysis: the results indicate that 97.7% of the degassed solid is MgO, the remaining material composed of small amounts of chloride and oxides of calcium, sulfur, silicon and iron (complete EDXRF data is given in Table S1 in the ESI).

Nitrogen adsorption and desorption isotherms were obtained to elucidate textural properties (graphs are presented in Figure S2 in the ESI). Altogether, the isotherms show typical type IV behavior, characteristic of mesoporous materials.⁵³ A specific surface area of 176.0 m² g⁻¹ was calculated by the Brunauer–Emmett–Teller (BET) method, and the Barret–Joyner–Halenda (BJH) method was used to calculate the total pore volume of 0.397 cm³ g⁻¹ and mean pore radius of 45.2 Å. In particular, it is important to note that the mean pore radius is significantly greater than the estimated kinetic radius of methyl paraoxon of 5.1 Å,⁴² facilitating the diffusion of bulk paraoxon toward the interior of the MgO pores. Additionally, the profile of pore radius distribution obtained by the BJH method indicate a small contribution of macropores (i.e., pores with radius greater than 250 Å).

The strength of the basic sites of MgO was evaluated by CO₂-TPD. Deconvolution of the profile of total CO₂ desorption as a function of temperature originates three CO₂ desorption peaks, corresponding to weak (20 - 160 °C), medium (160 - 400 °C) and strong (> 400 °C) basic sites.⁵⁴ Table 1 presents the total density of MgO basic sites and the values calculated for each deconvoluted peak. Note that the major contribution to the

Table 1 Base site density of MgO (μmol CO₂/g catalyst).

Total	785.3
Weak	238.3
Medium	197.1
Strong	349.9

total basicity of MgO is from strong basic sites, whose density corresponds to ca. 45% of the total, followed by weak and medium basic sites, with densities in the range 25–30% relative to the total value. It is worth to note that the total base density of MgO is some 3.5-fold greater than that of commercial γ -alumina (γ -Al₂O₃), a known weakly basic support (data shown in Table S5 in the ESI), which highlights the basic character of MgO.

Kinetic Measurements and Catalytic Activity

In order to evaluate the catalytic activity of MgO in the propanolysis of methyl paraoxon and understand the overall process in detail, we performed a thorough kinetic investigation by executing a series of reactions at different ratios of moles of substrate per mass unit of catalyst, lying between 5×10^{-6} and 5×10^{-3} mol g⁻¹ (substrate/catalyst) at 80 °C. Aliquots of the reaction media were withdrawn at appropriate time intervals and diluted in order to quantify spectrophotometrically the formation of the product *p*-nitrophenol as a function of time, and the data of fraction conversion against time were treated mathematically. Importantly, as shown later, experiments of LC-ESI-MS confirm that there is no side reaction, and thus the obtained kinetic profiles can be directly attributed to the substitution of *p*-nitrophenolate by 1-propanol.

When employing a constant amount of 300 mg of catalyst and varying the initial concentration of the substrate in the range of 0.0734 to 1.08 mM, first-order kinetics were observed, as indicated by the typical plot of fraction conversion against time in Figure 1A, obtained with 0.942 mM of the substrate (the complete set of kinetic data is shown in Figure S4 in the ESI). Thus, data of Figures 1A and S4 were fitted to eq. 1, in which *p*NP stands for the product *p*-nitrophenol, and k_1 is the observed first-order rate constant of the propanolysis reaction over the MgO surface.

$$\begin{aligned} (d[pNP]/dt) &= - (d[\text{methyl paraoxon}]/dt) = \\ &= k_1[\text{methyl paraoxon}] \end{aligned} \quad (1)$$

Differently from that observed in Figure 1A, results show that enlarging significantly the concentration of the substrate induces a change in the overall kinetic behavior. Figure 1B presents two related examples of kinetic profiles of reactions performed with 3 mg of MgO and concentrations of methyl paraoxon of 0.379 and 0.688 mM. At initial time intervals, when the MgO surface is exposed with active sites fully available for substrate adsorption, formation of the product *p*-nitrophenol obeys an exponential first order law, and then there is a change to a zero order process at longer times. Thus, such profiles were fitted to eq. 2, which is similar to eq. 1 and accounts for the zero order processes at longer times by the introduction of the k_2 term, a zero order rate constant. For the reaction performed at 0.379 mM of methyl paraoxon, a k_2 value of 5.43×10^{-10} M s⁻¹ is calculated and, consistently, a slightly lower value of 3.83×10^{-10} M s⁻¹ is obtained when using 0.688 mM of substrate. This scenario strongly suggests poisoning of the catalyst active sites by the substrate itself and/or the products dimethyl *n*-propyl phosphate and *p*-nitrophenol: the strong adsorption of the different species influences the progress of the reaction by affecting the catalyst surface, hindering the adsorption of further methyl paraoxon molecules onto the MgO surface, and

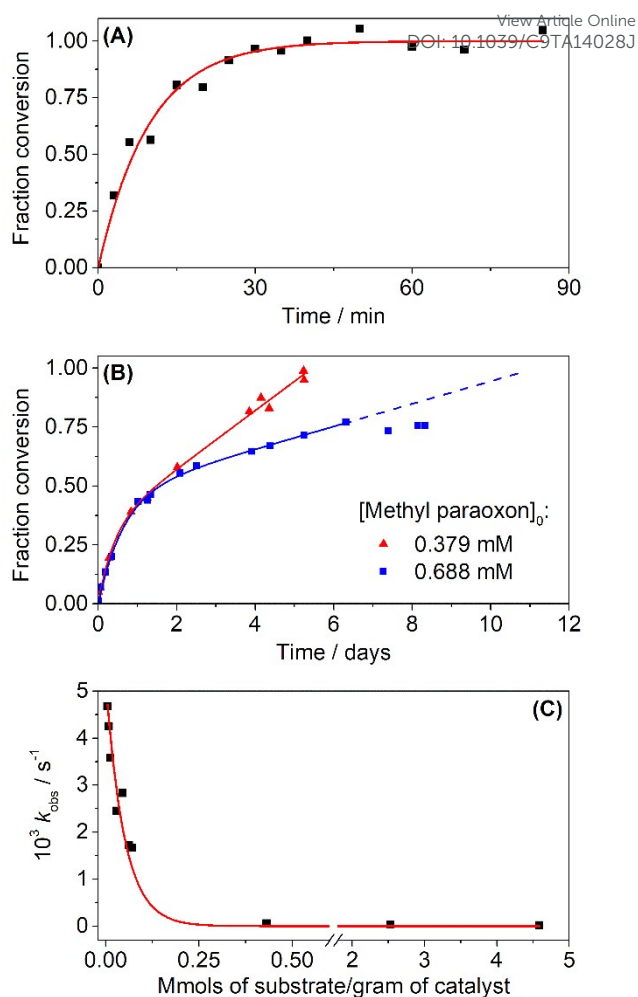


Figure 1 Kinetic data of the MgO-catalyzed propanolysis of methyl paraoxon, at 80°C. **(A)** Typical kinetic profile obtained when employing 300 mg of the catalyst and 0.942 mM of the substrate. Solid line represents fit to eq. 1. **(B)** Kinetic profiles obtained employing 3 mg of the catalyst and different amounts of the substrate, as indicated in the figure. Solid lines represent fit to eq. 2. **(C)** Data of k_{obs} as a function of the ratio of mmols of substrate per gram of catalyst.

consequently, lowering reaction rates and catalytic effects. In fact, it is possible to notice in Figure 1B that reaction goes to completion when employing 0.379 mM of methyl paraoxon in spite of the catalyst surface saturation. However, the same does not apply for the reaction with greater amount of the substrate: in the kinetics with 0.688 mM of methyl paraoxon, saturation of the catalyst surface occurs and allows conversion of up to ~75% of the substrate, as evidenced by the deviation of the three last experimental points at longer times from the expected course of the zero order process (dashed line). Most probably, saturation of the MgO catalyst surface is related to *p*-nitrophenol formation and its adsorption as the reaction proceeds, as also reported when employing mixed MgAl₂O₄ oxides and aluminum-titanate-supported erbium oxide as catalysts for methyl paraoxon propanolysis.^{42,44,45} Indeed, nitrophenols are known to present strong adsorption capabilities onto metal oxides in heterogeneous systems.⁵⁵

$$\begin{aligned} (d[\rho\text{NP}]/dt) &= - (d[\text{methyl paraoxon}]/dt) \\ &= k_1[\text{methyl paraoxon}] + k_2 \end{aligned} \quad (2)$$

Taking the first order rate constants for the kinetics as a function of the ratio of moles of substrate per gram of catalyst in the full range from 5×10^{-6} to 5×10^{-3} mol g^{-1} (substrate/catalyst), the plot of Figure 1C is obtained (for the kinetics that show surface saturation, the first order rate constant that describe the kinetics at initial time intervals were considered). In Figure 1C, it is observed an exponential decrease of the rate constants up to ca. 0.25 mmol g^{-1} (substrate/catalyst), followed by a plateau for larger ratios, a typical behavior expected for heterogeneously catalyzed reactions.^{30,31} Considering that the first order rate constant for the spontaneous propanolysis of methyl paraoxon is estimated to be $< 1.50 \times 10^{-9} \text{ s}^{-1}$,⁴² rate enhancements of up to 3×10^6 -fold can be obtained in the transesterification reaction by the proper choice of the experimental conditions: favoring lower substrate concentrations avoids active site overload by the substrate itself and/or adsorption of products and leads to greater catalytic activities.

Experiments of LC-ESI-MS

As described above, the MgO-mediated propanolysis of methyl paraoxon was followed spectrophotometrically and characteristic UV-Vis spectra of *p*-nitrophenolate were observed, suggesting that the reaction over the MgO surface proceeds through the nucleophilic attack of the solvent on the phosphorus of the substrate with *p*-nitrophenolate displacement. In order to confirm this reaction pathway, we performed LC-MS experiments to characterize in detail the reaction products, and the results show the formation of the phosphate triester dimethyl *n*-propyl phosphate as the transesterified product from the propanolysis of methyl paraoxon. Figure 2(A) shows a chromatogram obtained after

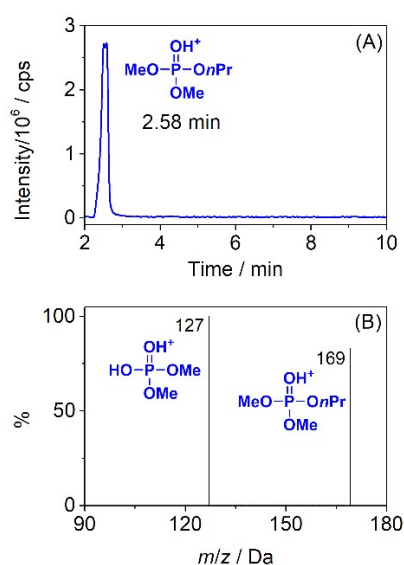


Figure 2 (A) Total ion current chromatogram of product ion of m/z 169, from an aliquot of the reaction medium of the MgO-catalyzed methyl paraoxon propanolysis at 4.61×10^{-5} mol g^{-1} (substrate/catalyst) after the reaction finished, and (B) respective ESI(+)-MS/MS of the ion of m/z 169 eluted at 2.58 min.

the propanolysis of methyl paraoxon with ESI(+)-MS detection, and it is observed the elution of the transesterified product at 2.58 minutes, whose ESI(+)-MS/MS characterization is shown in Figure 2(B).

In the ESI(+)-MS/MS of Figure 2(B) it is possible to identify the protonated dimethyl *n*-propyl phosphate of m/z 169 and the protonated species of dimethyl hydrogen phosphate of m/z 127, formed by the loss of $\text{CH}_2=\text{CH}_2\text{CH}_3$ from the species of m/z 169. The LC-MS results confirm the formation of dimethyl *n*-propyl phosphate and are in agreement with spectrophotometric observations, sustaining the reaction pathway outlined.

Adsorption calculations and mechanistic insights

In order to gain insight into the mechanism of methyl paraoxon transesterification with 1-propanol over the surface of the MgO catalyst, we performed DFT calculations and determined adsorption energies for the reactants. Provided that the reaction is heterogeneously catalyzed, adsorption of the reactants onto the oxide surface is an important, initial step of the overall catalytic cycle, thus evaluating their adsorption energies and detailed geometric parameters are indeed insightful, as well as the relative positioning of the reactants prior to the reaction, as discussed later. In our calculations, we used a slab model of the (100) surface of the bulk structure of periclase (MgO, Figure 3), in which a typical distance between adjacent surface oxygen atoms is 2.977 Å, while the typical surface cell O-O diagonal distance is 4.210 Å and similarly for Mg-Mg distances (Figure 3). The MgO (100) surface has been widely employed as a model in adsorption DFT calculations because of the simple theoretical description for such ionic, non-polar surface.^{56–58} Figure 3 also shows the geometries obtained for non-adsorbed methyl paraoxon and 1-propanol, while Figure 4 shows the final adsorbed structures obtained for the reactants. In all calculations, the MgO slab was composed of six atomic layers with the top three layers allowed to relax, while the bottom three were fixed, and we employed the

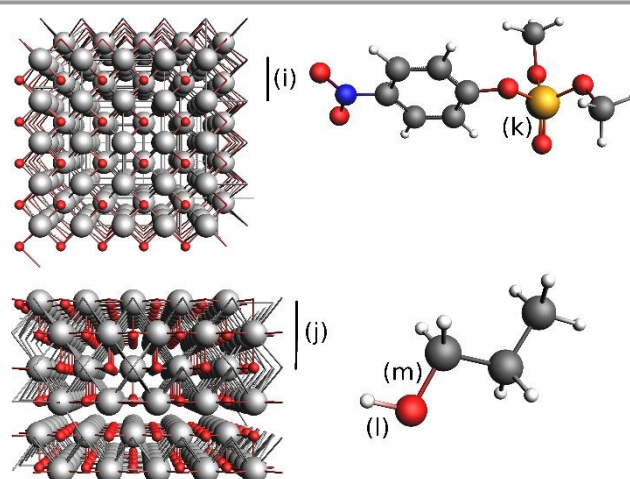


Figure 3 Phosphate educt (top right) and 1-propanol (bottom right) structures from gas phase optimization and (100) MgO surface model used (left). Selected geometry parameters are highlighted (Å): (i) typical $d(\text{Mg-Mg}) = d(\text{O-O}) = 2.977$, (j) typical $d(\text{Mg-Mg}) = 4.182$, $d(\text{O-O}) = 4.235$, (k) $d(\text{P=O}) = 1.482$, (l) $d(\text{O-H}) = 0.980$, (m) $d(\text{C-O}) = 1.448$.

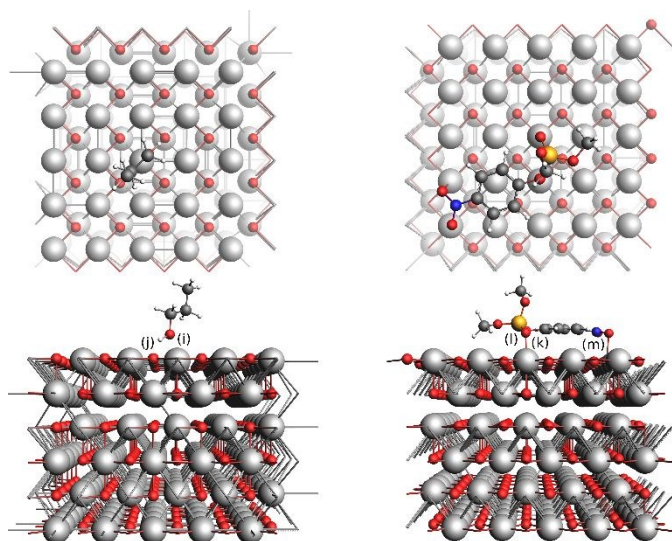


Figure 4 Top (top) and side view (bottom) of adsorbed 1-propanol (left) and phosphate educt (right). Selected geometry parameters are highlighted (Å): (i) $d(\text{O}\cdots\text{Mg}) = 2.159$, (j) $d(\text{OH}\cdots\text{O}) = 1.731$, (k) $d(\text{P}=\text{O}\cdots\text{Mg}) = 2.250$, (l) $d(\text{P}=\text{O}) = 1.492$, (m) $d(\text{NO}\cdots\text{Mg}) = 2.675$.

Grimme's D3 dispersion correction, as these have been shown to be adequate for calculations of adsorption energies when interactions between lone-pairs of adsorbates and surface Lewis acid sites play an important role.^{59–61}

1-Propanol adsorbs through its O-H group by interacting with a Mg-O group on the surface, in a structure that suggests dipole-dipole interactions together with hydrogen donation to the surface (Figure 4). The O \cdots Mg contact obtained was 2.159 Å, while OH \cdots O amounts to 1.731 Å. Furthermore, while the O-H bond of 1-propanol elongates upon adsorption ($d(\text{O-H})$ increases from 0.980 to 1.010 Å), its C-O bond shortens ($d(\text{C-O})$ decreases from 1.448 to 1.431 Å).

The phosphate educt adsorption was modeled through a P=O \cdots Mg contact, which amounted to 2.250 Å (Figure 4). A NO \cdots Mg contact, from the nitro group of the ring to the surface, was also observed ($d(\text{NO}\cdots\text{Mg}) = 2.675$ Å). We also observe a small elongation of the P=O distance upon adsorption (from 1.482 to 1.492 Å), as well as an elongation of the Ph-O bond of the leaving group (from 1.387 to 1.403 Å).

Adsorption energies for 1-propanol and the phosphate educt were found to be -18.4 and -57.9 kcal/mol, respectively, which suggests that 1-propanol binds less strongly to the surface than methyl paraoxon. Furthermore, the phosphate product showed a smaller adsorption energy (-36.9 kcal/mol) than the educt (Figure S12). In order to estimate the relationship of reactive sites of the surface, Figure 5 shows an approximate distance map of the surface, created by simple translation of the optimized 1-propanol structure around the surface, while keeping the phosphate educt static at the origin, where each dot represents a Mg adsorption site. Since the adsorption of both reactants on the same Mg²⁺ site is precluded by steric reasons (in this case, $d(\text{O}\cdots\text{P}) = 1.419$ Å), the shortest possible distance between the two educts is around 2.4 Å, when the reactants are adsorbed on adjacent Mg sites (Figure 5).

Altogether, the experimental and theoretical results provide

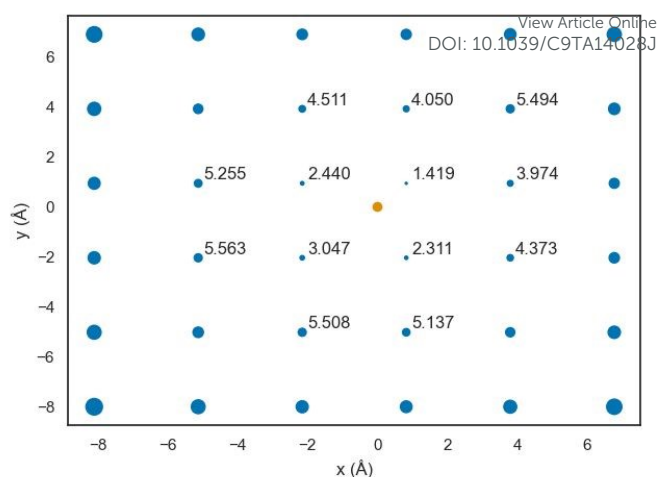


Figure 5 Distance map for adsorbed reactants, in which the orange dot represents the phosphate educt and the blue dots represent different adsorption sites for 1-propanol. Numbers represent the smallest $d(\text{O}\cdots\text{P})$ distances between reactive groups. Dot sizes are proportional to the square of the distances.

significant insights into a better comprehension of the overall catalytic process from a mechanistic point of view. In this sense, the reactants adsorb on the catalyst surface, where the transesterification takes place and leads to the formation of dimethyl *n*-propyl phosphate and 4-nitrophenol, and then the products should desorb from the MgO surface in order to regenerate the catalyst surface. In particular, the DFT calculations enlighten that the reaction most probably occurs when the reactants are found at adjacent Mg²⁺ sites, where the distance between the nucleophilic and electrophilic centers is ca. 2.4 Å. On the basis of the general scheme for phosphoryl transfer reactions from phosphate triesters to oxygen nucleophiles,^{62–64} and considering the basic character of the MgO surface, the reaction should thus be favored by base catalysis promoted by the catalyst surface, assisting nucleophilic attack of 1-propanol on a juxtapositioned methyl paraoxon molecule. This argument is in agreement with the optimized structure for the proton dissociation from 1-propanol over the MgO surface, which readily converged back to the 1-propanol structure (a structure comparison is shown in Figure S13). Thus, the probable adsorbed structure is 1-propanol and not 1-propoxide, allowing the consideration that the latter should only be formed as an incipient species along the reaction coordinate, leading to either a short-lived phosphorane intermediate or directly to the products through a single transition state.

Catalyst recycling

Focusing on one of the greatest advantages of heterogeneous catalysis, the reuse of the catalyst, we evaluated the activity of the MgO employed in the propanolysis of methyl paraoxon at a ratio of 4.6×10^{-5} mol g⁻¹ (substrate/catalyst) in two further sequential reactions. Provided that the products may adsorb onto the catalyst surface, *p*-nitrophenol in particular, the utilized MgO was subjected to a washing reactivation treatment

between the reactions looking for the full recovery of the MgO active sites (for details, see Experimental Section). First order rate constants were calculated from the kinetic data of the three sequential reactions, and we obtained 2.83×10^{-3} , 2.09×10^{-3} and $1.95 \times 10^{-3} \text{ s}^{-1}$, and within experimental error, these values show that there was no loss of catalytic activity of the MgO in the propanolysis of methyl paraoxon.

Importantly, we performed post-characterization experiments to evaluate possible interference of the reactivation process in the structure and properties of MgO. TGA analysis after the first cleaning procedure of MgO show a mass reduction of 5% with increasing temperature up to 300 °C (TGA profile shown in Figure S6 in the ESI). Differently from that observed in the semi-quantitative EDXRF analysis before the first use, the MgO reactivated after the second use shows the presence of 0.5% of Na₂O in the degassed material, a result that indicates trace amounts of NaCl as a residue from the reactivation procedure without promoting significant modifications in the original structure of MgO (complete EDXRF data is shown in Table S3 in the ESI). Though the ionic radius of sodium is greater than that of magnesium, which hinders the incorporation of sodium into the MgO structure,⁶⁵ the presence of sodium could eventually obstruct the catalyst pores, resulting in lower surface area.^{66–69}

Textural properties of the reactivated MgO after the third use show a reduction of c.a. 35% of the specific surface area ($S_{\text{BET}} = 114.3 \text{ m}^2 \text{ g}^{-1}$), compared to that of MgO before the first use, which did not influence significantly the catalytic activity, as shown by the above comparison of the first order rate constants. The decrease of the specific surface area could be an effect of the successive procedures for reactivating the catalyst and for its thermic activation prior to the reactions, the latter possibly resulting in the generation of active phases and sintering processes,⁷⁰ for example. Additionally, the recycled MgO mean pore radius was determined to be 65.3 Å, a value that is c.a. 45% greater compared to that of the original MgO, indicating that the diffusion of bulky methyl paraoxon onto the catalyst active sites is still allowed. Lastly, volume pore of recycled MgO was $0.373 \text{ cm}^3 \text{ g}^{-1}$, a value c.a. 6% lower than that of the original catalyst.

Finally, evaluation of MgO basicity after its third use was performed by CO₂-TPD, and the results show a total base density of $364.1 \mu\text{mol CO}_2/\text{g}$ of catalyst, from which 226.5, 79.4 and $58.2 \mu\text{mol CO}_2/\text{g}$ of catalyst are discriminated as weak, medium and strong base site density, respectively. Though a reduction of c.a. 46% of the total base density of MgO is observed in comparison to the scenario prior to the first use, it seems that the basicity is still enough for the reaction without loss of catalytic activity. Actually, MgO total base density after third use is still satisfactory, being superior to the weakly basic $\gamma\text{-Al}_2\text{O}_3$ support, for instance (see Table S5 in the ESI). Furthermore, it is important to notice that the catalytic activity of a solid material is rarely explained by means of one single aspect, and generally several properties contribute simultaneously to the catalytic efficiency. Thus, the MgO properties after the third use seem to be sufficient altogether to maintain the initial catalytic activity observed in the methyl

paraoxon propanolysis, allowing the conduction of the adsorptive transesterification.

DOI: 10.1039/C9TA14028J

MgO-mediated propanolysis of dialkyl aryl and triaryl phosphate triesters

Since MgO showed to be highly active towards the transesterification of methyl paraoxon, we evaluated the catalytic activity of MgO towards the propanolysis of a range of representative dialkyl aryl and triaryl phosphate triesters, whose structures are shown in Chart 1. The reactions were performed under the optimized experimental conditions for the propanolysis of methyl paraoxon, and the kinetics were similarly followed spectrophotometrically in order to quantify the formation of the phenolic product as a function of time.

For the propanolysis of the dialkyl aryl phosphate triesters, typical first order kinetic profiles were obtained, similar to the scenario described for methyl paraoxon, and thus the data for such substrates were fitted to an equation of the type of eq. 1. First order rate constants obtained are presented in Table 2, along the rate enhancements, which highlight that MgO effectively promotes the transesterification of the three substrates. LC-MS analyses of aliquots of the reaction media after the reactions have finished show that a trialkyl phosphate ester is obtained, either dimethyl *n*-propyl phosphate or diethyl *n*-propyl phosphate (representative LC-MS data is shown in Figure S7 in the ESI).

Interestingly, the absorbance changes in the kinetic profiles of the propanolysis of the triaryl phosphates are as much as two or three times greater than that expected for the substitution of only one of the aromatic substituents for the T2PyP and

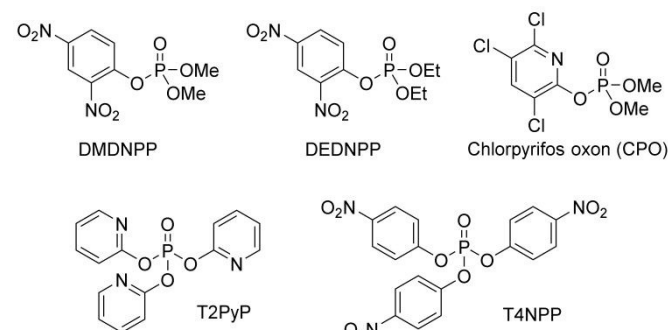


Chart 1 Phosphate triesters subjected to propanolysis over MgO.

Table 2 Rate constants, transesterified products and rate enhancements for the propanolysis of dialkyl aryl phosphate esters catalyzed by MgO at $4.61 \times 10^{-5} \text{ mol g}^{-1}$ (substrate/catalyst), at 80 °C.

Substrate	$k_1, \text{ s}^{-1}$	Transesterified product	k_1/k_0^a
DMDNPP	5.13×10^{-3}	dimethyl <i>n</i> -propyl phosphate	3.56×10^4
DEDNPP	3.10×10^{-3}	diethyl <i>n</i> -propyl phosphate	3.88×10^2
CPO	2.09×10^{-3}	dimethyl <i>n</i> -propyl phosphate	3.43×10^3

^a k_0 refers to the spontaneous solvolysis first order rate constants of the substrates as benchmarks: propanolysis, in the case of DMDNPP, estimated by the initial velocity method, and hydrolysis, for DEDNPP and CPO, obtained from literature.^{44,71}

T4NPP substrates, respectively. Thus the kinetic profiles can not be appropriately fitted to a monoexponential first order equation, as shown in Figure 6. These observations indicate that two or three aromatic moieties of the substrate are substituted by 1-propanol in two or three consecutive first order transesterification reactions, as depicted in Scheme 2, with rate constants significantly different. Thus, the kinetic profiles were fitted to equations in which the absorbance at a given time is related to the sum of the concentrations of phenolic product arising from the first, second, and third step, when applicable (equations are given in the ESI).

Table 3 presents the first order rate constants k_1 , k_2 and k_3 , which refer to the first, second and third steps, respectively, in the propanolysis of the triaryl substrates. Table 3 shows that the rate constant for the substitution reaction of one aromatic substituent (first step, k_1) is up to c.a. 5×10^4 -fold greater than those of the spontaneous propanolysis of the substrates. Interestingly, it is worth noting that the time required for the substitution of two aromatic substituents in the T2PyP by 1-propanol is c.a. 750-fold lower than that required for the substitution of solely the first equivalent in the spontaneous

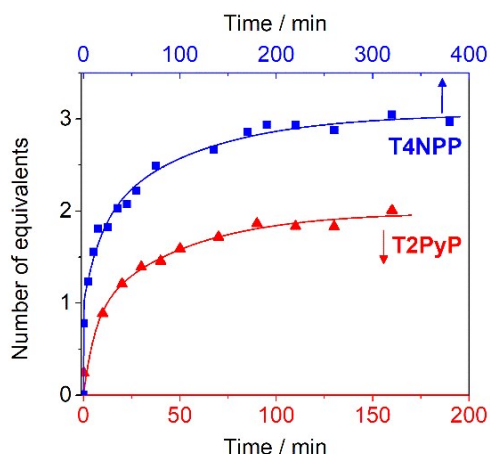
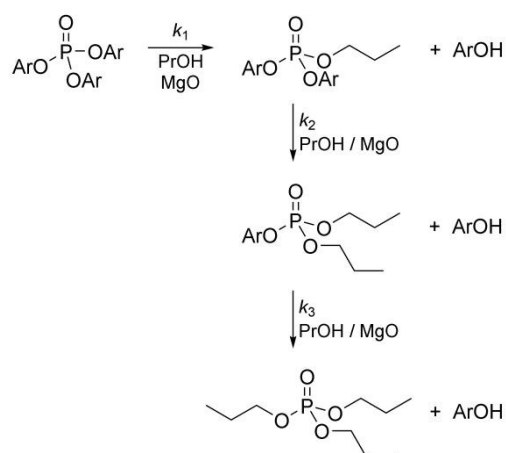


Figure 6 Kinetics of the propanolysis reactions of T2PyP and T4NPP catalyzed by MgO, both at $4.6 \times 10^{-5} \text{ mol g}^{-1}$ (substrate/catalyst), at 80°C . The concentration of the aromatic product was expressed in the y-axis as the number of equivalents relative to the substrate.



Scheme 2 Successive propanolysis reactions observed with triaryl substrates. OAr represents an aromatic substituent of the phosphate triester.

Table 3 Rate constants, transesterified products and rate enhancements for the propanolysis of triaryl phosphate esters catalyzed by MgO at $4.6 \times 10^{-5} \text{ mol g}^{-1}$ (substrate/catalyst), at 80°C .

Rate constants (s^{-1})	Transesterified products	k_1/k_0^c
T2PyP ^a		
$k_1 = 2.79 \times 10^{-3}$	<i>bis</i> -2-pyridyl <i>n</i> -propyl phosphate	6.17×10^3
$k_2 = 3.40 \times 10^{-4}$	2-pyridyl <i>bis</i> - <i>n</i> -propyl phosphate	–
T4NPP		
$k_1 \geq 7.15 \times 10^{-2}$ ^b	<i>bis</i> -4-nitrophenyl <i>n</i> -propyl phosphate	5.14×10^4
$k_2 = 9.36 \times 10^{-4}$	4-nitrophenyl <i>bis</i> - <i>n</i> -propyl phosphate	–
$k_3 = 1.55 \times 10^{-4}$	<i>tris</i> - <i>n</i> -propyl phosphate	–

^a LC-MS analyses show that the third step does not occur to a significant extent for the T2PyP substrate in the time domain at which the reaction was followed. ^b Must be rather considered as a minimum value, since the first reaction was too fast to collect enough experimental points in its time domain. ^c k_0 refers to the spontaneous propanolysis first order rate constants of the substrates, estimated by the initial velocity method.

solvolysis of the substrate, evidencing the high activity of MgO toward successive transesterification reactions of organophosphate esters. In the case of the T4NPP substrate, the time required for substitution of the three aromatic aromatic moieties is some 100-fold lower compared to that for the spontaneous substitution of just the first substituent.

Experiments of LC-ESI-MS in the positive ion mode are in agreement with the proposed pathways of Scheme 2. For example, from a chromatographic separation of the reactants, intermediate and products in the MgO-catalyzed propanolysis of the T2PyP at approximately 40 min, it is possible to extract the chromatograms of Figure 7(A) that show the elution of the species with m/z 317 and 282, consistent with the sodium adducts of *n*-propyl *bis*-2-pyridyl phosphate and *bis*-*n*-propyl 2-pyridyl phosphate, respectively. Additionally, the identification of the above mentioned phosphates is confirmed by the ESI(+)-MS spectra of the products. In the spectrum of the product eluted at 3.24 min, Figure 7(B), besides the sodium adduct of the *n*-propyl *bis*-2-pyridyl phosphate, it is observed the ion of m/z 295, consistent with a protonated species of the triester, and the ion of m/z 253, formed by the loss of $\text{CH}_3\text{CH}_2=\text{CH}_2$ from the ion of m/z 295. Similarly, the ESI(+)-MS spectrum of the product eluted at 3.45 min, Figure 7(C), is fully consistent with the formation of the *bis*-*n*-propyl 2-pyridyl phosphate, the species with m/z 282 and 260 being consistent with the sodium adduct and the protonated species of the triester, respectively. In Figure 7(C), it is also possible to identify the species of m/z 218 and 176, formed by the loss of one and two $\text{CH}_3\text{CH}_2=\text{CH}_2$ groups, respectively, from the m/z 260. This attribution is consistent by the ESI(+)-MS/MS spectrum obtained for the ion of m/z 260 (Figure S8 in the ESI).

4. Conclusions

Herein, we reported the propanolysis of methyl paraoxon catalyzed by a commercial magnesium oxide at 80°C . A series of kinetic experiments with varying ratios of moles of substrate

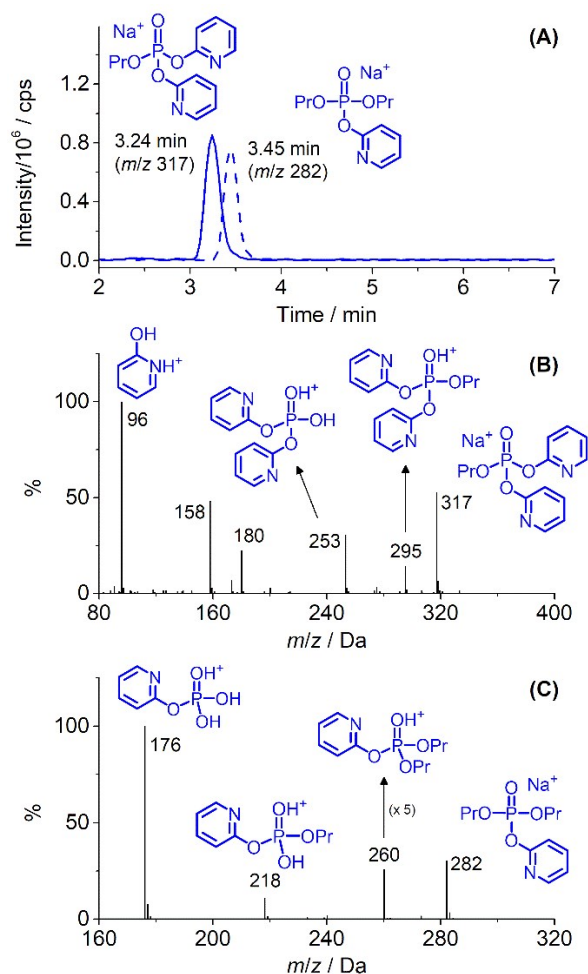


Figure 7 (A) Extracted ion chromatograms of the species of m/z 317 and 282 from an aliquot of the reaction medium of the MgO-catalyzed propanolysis of T2PyP, obtained by LC-ESI(+)-MS, and complete ESI(+)-MS spectra of the products eluted at: (B) 3.24 min, and (C) 3.45 min.

per mass unit of catalyst was performed, in the range 5×10^{-6} to 5×10^{-3} mol g^{-1} (substrate/catalyst), and the results showed that rate enhancements up to 3×10^6 -fold can be obtained depending upon the experimental conditions, in comparison with the spontaneous propanolysis of the substrate. The MgO-catalyzed propanolysis of methyl paraoxon leads to the formation of dimethyl *n*-propyl phosphate in a process that converts a toxic organophosphate into a phosphate triester structurally analogous to a family of flame-retardant compounds. Additionally, MgO could be reactivated through a simple washing procedure, maintaining its catalytic activity when employed in two additional sequential batches. Furthermore, MgO presented high catalytic activity toward the transesterification of a series of phosphate triesters, and in the particular case of triaryl substrates, successive transesterification reactions were observed.

Although our system is heterogeneous, the catalytic effects promoted by MgO in the propanolysis of methyl paraoxon can be nicely viewed in light of the spatiotemporal theory for intramolecular reactions of organic molecules in solution.^{72–76} In this approach, reactive groups are considered to be caged at so-

called *contact distances*, which are usually shorter than solvent diameter, with the observed reactivity ascribed to the persistent interaction between the functionalities (provided they are found at appropriate geometries) overcoming the time required for reactants to diffuse and collide effectively in the corresponding bimolecular counterpart. Thus, in our system, besides the fact that the acid Mg^{2+} sites could facilitate the reaction by enhancing the substrate electrophilicity and/or stabilizing partial negative charges along the reaction coordinate,⁶⁴ an important part of the catalytic efficiency should be consequence of the ability of the MgO surface to offer *adjacent* Mg^{2+} sites: this allows for the juxtapositioning of the reactants for persistent interaction at adequate distances, as supported by the distance map obtained by DFT calculations.

Additionally, the basicity is clearly important to explain the MgO catalytic efficiency contributing with a significant increase in reactivity of the nucleophile. To test this hypothesis, we performed a set of kinetics with the weakly basic γ - Al_2O_3 to evaluate its catalytic activity towards the propanolysis of methyl paraoxon (complete results of commercial γ - Al_2O_3 characterization and kinetic data are shown in the ESI). The largest first order rate constant obtained for the reaction in the presence of γ - Al_2O_3 was $1.20 \times 10^{-4} s^{-1}$ at a ratio of 4.6×10^{-5} mol g^{-1} (substrate/catalyst), a rate constant which is some 24-fold lower than the calculated first order rate constant of $2.83 \times 10^{-3} s^{-1}$ for the reaction over the MgO surface at same ratio of substrate moles/catalyst mass. Provided that γ - Al_2O_3 and MgO present similar textural properties, but MgO base site density is c.a. 3.5-fold greater, this result is a good indication of the importance of basicity as a factor to explain the greater catalytic activity of MgO toward methyl paraoxon propanolysis. More basic surfaces facilitate proton abstraction and nucleophilic attack upon the phosphorus atom.

Since MgO is shown to be significantly active in the propanolysis of a range of phosphate triesters besides methyl paraoxon, the results are encouraging for the design of novel efficient solid catalysts for targeted transesterification processes. In addition to convenient textural properties, basicity seems to play an important role in the efficiency of metal oxides in catalyzing the propanolysis of phosphate triesters, highlighting the importance of the exploration of the solids' properties in the continuing design of simple metal oxide catalysts.

Conflicts of interest

There are no conflicts to declare.

Acknowledgements

We dedicate this paper to Prof. Faruk Nome, deceased since September 24, 2018, who dedicated more than five decades to teaching and research. With his enthusiasm for science, he became a paragon of commitment to research among his colleagues and collaborators, leaving a legacy that will certainly be transmitted to generations of students to come. The authors

thank the Brazilian funding agencies CNPq, Capes and FAPESC, and the National Institute of Science and Technology in Molecular and Nanostructured Systems (INCT-Catálise). E.H.W thanks São Paulo Research Foundation (FAPESP, grant #2019/07899-5). G.F.C. thanks CNPq (grant 311963/2017-0) for the research fellowship, and F. S. S. S. thanks CNPq for a PhD scholarship (grant 140485/2017-1).

Notes and references

- Y. J. Jang, K. Kim, O. G. Tsay, D. A. Atwood and D. G. Churchill, *Chem. Rev.*, 2015, **115**, PR1–PR76.
- S. Costanzi, J.-H. Machado and M. Mitchell, *ACS Chem. Neurosci.*, 2018, **9**, 873–885.
- G. Mercey, T. Verdet, J. Renou, M. Kliachyna, R. Baati, F. Nachon, L. Jean and P.-Y. Renard, *Acc. Chem. Res.*, 2012, **45**, 756–766.
- B. M. Smith, *Chem. Soc. Rev.*, 2008, **37**, 470–478.
- A. M. Manfredi, W. Demos, E. H. Wanderlind, B. V. Silva, A. C. Pinto, B. S. Souza and F. Nome, *Journal of Physical Organic Chemistry*, 2016, **29**, 600–603.
- B. Picard, I. Chataigner, J. Maddaluno and J. Legros, *Org. Biomol. Chem.*, 2019, **17**, 6528–6537.
- G. Kaur, A. Singh, A. Singh, N. Kaur and N. Singh, *Dalton Trans.*, 2018, **47**, 5595–5606.
- D. Millán, R. A. Tapia and P. Pavez, *Front. Chem.*, 2019, **6**, 669.
- A. Singh, P. Raj, A. Singh, J. J. Dubowski, N. Kaur and N. Singh, *Inorg. Chem.*, 2019, **58**, 9773–9784.
- Y. Tian, A. M. Plonka, A. M. Ebrahim, R. M. Palomino, S. D. Senanayake, A. Balboa, W. O. Gordon, D. Troya, D. G. Musaeov, J. R. Morris, M. B. Mitchell, D. L. Collins-Wildman, C. L. Hill and A. I. Frenkel, *J. Phys. Chem. Lett.*, 2019, **10**, 2295–2299.
- D. Zhang, W. Zhang, Z. Lin, J. Dong, N. Zhen, Y. Chi and C. Hu, *Inorg. Chem.*, 2020, **59**, 9756–9764.
- J. Czescik, Y. Lyu, S. Neuberg, P. Scrimin and F. Mancin, *J. Am. Chem. Soc.*, 2020, **142**, 6837–6841.
- L. Bromberg, W. R. Creasy, D. J. McGarvey, E. Wilusz and T. A. Hatton, *ACS Appl. Mater. Interfaces*, 2015, **7**, 22001–22011.
- K. P. Sullivan, W. A. Neiwert, H. Zeng, A. K. Mehta, Q. Yin, D. A. Hillesheim, S. Vivek, P. Yin, D. L. Collins-Wildman, E. R. Weeks, T. Liu and C. L. Hill, *Chem. Commun.*, 2017, **53**, 11480–11483.
- A. P. Gerola, E. H. Wanderlind, Y. S. Gomes, L. A. Giusti, L. Garcia-Rio, R. A. Nome, A. J. Kirby, H. D. Fiedler and F. Nome, *ACS Catal.*, 2017, **7**, 2230–2239.
- N. Karton-Lifshin, S. Katalan, I. Columbus, R. Chen, L. Yehezkel, M. Madmon, S. Dagan, S. Elias, G. Fridkin and Y. Zafrani, *Chem. Commun.*, 2019, **55**, 12471–12474.
- E. H. Wanderlind, C. R. Bittencourt, A. M. Manfredi, A. P. Gerola, B. S. Souza, H. D. Fiedler and F. Nome, *J. Phys. Org. Chem.*, 2019, e3837.
- L. Gabrielli, L. J. Prins, F. Rastrelli, F. Mancin and P. Scrimin, *Eur. J. Org. Chem.*, 2020, Early View. DOI: 10.1002/ejoc.202000356.
- F. Fan, Y. Zheng, Y. Zhang, H. Zheng, J. Zhong and Z. Cao, *ACS Catal.*, 2019, **9**, 7038–7051.
- J. E. Forman and C. M. Timperley, *Curr. Opin. Green Sustainable Chem.*, 2019, **15**, 103–114.
- A. N. Bigley, T. Narindoshvili, D. F. Xiang and F. M. Raushel, *Biochemistry*, 2020, **59**, 1273–1288.
- C. A. A. Vargas, J. I. dos Santos, C. C. Nascentes, A. M. L. Denadai, M. H. Araujo and T. A. S. Brandão, *Microporous Mesoporous Mater.*, 2018, **268**, 144–152.
- J. Henych, A. Mattsson, J. Tolasz, V. Štengl and L. Österlund, *Catal. Sci. Technol.*, 2019, **9**, 1816–1824.
- S.-W. Zhan, W.-B. Tseng and W.-L. Tseng, *Environmental Research*, 2020, **188**, 109653. DOI: 10.1039/C9TA14028J
- R. Ruschel Campedelli, M. H. Keller, G. Pinheiro, C. E. M. Campos, L. Zaramello and B. Silveira de Souza, *J. Org. Chem.*, 2019, **84**, 9975–9983.
- J. Lee, E.-Y. Kim, B.-J. Chang, M. Han, P.-S. Lee and S.-Y. Moon, *Journal of Membrane Science*, 2020, **605**, 118112.
- K. O. Kirlikovali, Z. Chen, T. Islamoglu, J. T. Hupp and O. K. Farha, *ACS Appl. Mater. Interfaces*, 2020, **12**, 14702–14720.
- S. F. Blaskiewicz, W. G. Endo, A. J. G. Zarbin and E. S. Orth, *Applied Catalysis B: Environmental*, 2020, **264**, 118496.
- C. A. Walenta, F. Xu, C. Tesvara, C. R. O'Connor, P. Sautet and C. M. Friend, *J. Phys. Chem. C*, 2020, **124**, 12432–12441.
- R. L. Augustine, *Heterogeneous catalysis for the synthetic chemist*, M. Dekker, New York, 1996.
- G. Rothenberg, *Catalysis: concepts and green applications*, WILEY-VCH, Weinheim, 2008.
- A. S. P. Lovón, J. J. Lovón-Quintana, G. I. Almerindo, G. P. Valença, M. I. B. Bernardi, V. D. Araújo, T. S. Rodrigues, P. A. Robles-Dutenhefner and H. V. Fajardo, *Journal of Power Sources*, 2012, **216**, 281–289.
- J. J. Spivey, K. S. Krishna, C. S. S. R. Kumar, K. M. Dooley, J. C. Flake, L. H. Haber, Y. Xu, M. J. Janik, S. B. Sinnott, Y.-T. Cheng, T. Liang, D. S. Sholl, T. A. Manz, U. Diebold, G. S. Parkinson, D. A. Bruce and P. de Jongh, *J. Phys. Chem. C*, 2014, **118**, 20043–20069.
- G. W. Wagner, P. W. Bartram, O. Koper and K. J. Klabunde, *J. Phys. Chem. B*, 1999, **103**, 3225–3228.
- G. W. Wagner, O. B. Koper, E. Lucas, S. Decker and K. J. Klabunde, *J. Phys. Chem. B*, 2000, **104**, 5118–5123.
- A. Michalkova and J. Leszczynski, *J. Vac. Sci. Technol., A*, 2010, **28**, 1010–1017.
- G. W. Wagner, G. W. Peterson and J. J. Mahle, *Ind. Eng. Chem. Res.*, 2012, **51**, 3598–3603.
- R. S. Alvim, V. S. Vaiss, A. A. Leitão and I. Borges, *J. Phys. Chem. C*, 2013, **117**, 20791–20801.
- L. Y. Kuo, A. Bennett and Q. Miao, *Inorg. Chem.*, 2017, **56**, 10013–10020.
- I. O. Kady, *Chem. Lett.*, 2008, **37**, 744–745.
- D. P. Sheng and I. O. Kady, *Appl. Catal., A*, 2009, **365**, 149–152.
- L. M. Zimmermann, G. I. Almerindo, J. R. Mora, I. H. Bechtold, H. D. Fiedler and F. Nome, *J. Phys. Chem. C*, 2013, **117**, 26097–26105.
- M. Venier, A. Salamova and R. A. Hites, *Acc. Chem. Res.*, 2015, **48**, 1853–1861.
- L. M. Zimmermann, G. I. Almerindo, M. Medeiros, R. F. Affeldt, E. H. Wanderlind, A. P. Gerola, R. A. Nome, M. A. Tumelero, R. Faccio, A. A. Pasa, H. D. Fiedler and F. Nome, *J. Phys. Chem. C*, 2018, **122**, 25530–25538.
- G. I. Almerindo, P. Bueno, L. M. Nicolazi, E. H. Wanderlind, P. Sangaletti, S. M. Landi, L. A. Sena, B. S. Archanjo, C. A. Achete, H. D. Fiedler and F. Nome, *J. Phys. Chem. C*, 2016, **120**, 22323–22329.
- J. V. Hemmer, E. W. Wanderlind, H. A. G. Bazani, C. E. M. Campos, T. M. Wagner, A. K. Emmerich, J. R. U. Adão and G. I. Almerindo, *Braz. J. Chem. Eng.*, 2020, Just Accepted. DOI: 10.1007/s43153-020-00048-4.
- D18 Committee, *D2216. Test Methods for Laboratory Determination of Water (Moisture) Content of Soil and Rock by Mass*, ASTM International, 2010.
- H. D. Fiedler, E. E. Drinkel, B. Orzechowicz, E. C. Leopoldino, F. D. Souza, G. I. Almerindo, C. Perdona and F. Nome, *Anal. Chem.*, 2013, **85**, 10142–10148.
- E. P. Barrett, L. G. Joyner and P. P. Halenda, *J. Am. Chem. Soc.*, 1951, **73**, 373–380.
- Y. Zhang and W. Yang, *Phys. Rev. Lett.*, 1998, **80**, 890–890.
- G. te Velde, F. M. Bickelhaupt, E. J. Baerends, C. Fonseca

- Guerra, S. J. A. van Gisbergen, J. G. Snijders and T. Ziegler, *J. Comput. Chem.*, 2001, **22**, 931–967.
- 52 R. M. Hazen, *Am. Mineral.*, 1976, **61**, 266–271.
- 53 K. S. W. Sing, *Pure Appl. Chem.*, 1985, **57**, 603–619.
- 54 M. A. Aramendia, V. Borau, C. Jiménez, J. M. Marinas, J. R. Ruiz and F. J. Urbano, *Appl. Catal., A*, 2003, **244**, 207–215.
- 55 S. Chen, Z. P. Xu, Q. Zhang, G. Q. M. Lu, Z. P. Hao and S. Liu, *Sep. Purif. Technol.*, 2009, **67**, 194–200.
- 56 G. Barcaro and A. Fortunelli, *J. Chem. Theory Comput.*, 2005, **1**, 972–985.
- 57 G. Barcaro, E. Aprà and A. Fortunelli, *Chem. Eur. J.*, 2007, **13**, 6408–6418.
- 58 Z. Mao, W. Zhao, Z. A. Al-Mualem and C. T. Campbell, *J. Phys. Chem. C*, 2020, **124**, 14685–14695.
- 59 A. Kakekhani, L. T. Roling, A. Kulkarni, A. A. Latimer, H. Abroshan, J. Schumann, H. AlJama, S. Siahrostami, S. Ismail-Beigi, F. Abild-Pedersen and J. K. Nørskov, *Inorg. Chem.*, 2018, **57**, 7222–7238.
- 60 A. A. Latimer, A. Kakekhani, A. R. Kulkarni and J. K. Nørskov, *ACS Catal.*, 2018, **8**, 6894–6907.
- 61 S. Grimme, S. Ehrlich and L. Goerigk, *J. Comput. Chem.*, 2011, **32**, 1456–1465.
- 62 A. J. Kirby, M. Medeiros, P. S. M. Oliveira, E. S. Orth, T. A. S. Brandão, E. H. Wanderlind, A. Amer, N. H. Williams and F. Nome, *Chemistry - A European Journal*, 2011, **17**, 14996–15004.
- 63 M. Medeiros, E. H. Wanderlind, J. R. Mora, R. Moreira, A. J. Kirby and F. Nome, *Organic & Biomolecular Chemistry*, 2013, **11**, 6272.
- 64 A. J. Kirby and F. Nome, *Acc. Chem. Res.*, 2015, **48**, 1806–1814.
- 65 J. Barrault, Y. Pouilloux, J. M. Clacens, C. Vanhove and S. Bancquart, *Catal. Today*, 2002, **75**, 177–181.
- 66 S. Szczepaska and S. Malinowski, *J. Catal.*, 1969, **15**, 68–82.
- 67 W. D. Mross, *Catal. Rev.*, 1983, **25**, 591–637.
- 68 V. Perrichon and M. C. Durupty, *Appl. Catal.*, 1988, **42**, 217–227.
- 69 A. D’Cruz, M. G. Kulkarni, L. C. Meher and A. K. Dalai, *J. Am. Oil Chem. Soc.*, 2007, **84**, 937–943.
- 70 M. Campanati, G. Fornasari and A. Vaccari, *Catal. Today*, 2003, **77**, 299–314.
- 71 E. H. Wanderlind, E. S. Orth, M. Medeiros, D. M. P. O. Santos, E. Westphal, H. Gallardo, H. D. Fiedler and F. Nome, *J. Braz. Chem. Soc.*, 2014, **25**, 2385–2391.
- 72 B. S. Souza, J. R. Mora, E. H. Wanderlind, R. M. Clementin, J. C. Gesser, H. D. Fiedler, F. Nome and F. M. Menger, *Angew. Chem., Int. Ed.*, 2017, **56**, 5345–5348.
- 73 E. H. Wanderlind, D. G. Liz, A. P. Gerola, R. F. Affeldt, V. Nascimento, L. C. Bretanha, R. Montecinos, L. Garcia-Rio, H. D. Fiedler and F. Nome, *ACS Catal.*, 2018, **8**, 3343–3347.
- 74 E. V. Silveira, V. Nascimento, E. H. Wanderlind, R. F. Affeldt, G. A. Micke, L. Garcia-Rio and F. Nome, *J. Org. Chem.*, 2019, **84**, 9684–9692.
- 75 L. Scorsin, R. F. Affeldt, B. S. Oliveira, E. V. Silveira, M. S. Ferraz, F. P. S. de Souza, G. F. Caramori, F. M. Menger, B. S. Souza and F. Nome, *J. Org. Chem.*, 2020, **85**, 4663–4671.
- 76 F. M. Menger and F. Nome, *ACS Chem. Biol.*, 2019, **14**, 1386–1392.

View Article Online
DOI: 10.1039/C9TA14028J